GOLD Observations of Equatorial Plasma Bubbles Reaching Mid-Latitudes During the 23 April 2023 Geomagnetic Storm

Deepak Kumar Karan[1], Carlos R. Martinis[2], Richard W. Eastes[1], Robert E. Daniell[3], William E. McClintock[1] and Chao-Song Huang[4]

[1]Laboratory for Atmospheric and Space Physics, University of Colorado, Boulder, CO, USA

[2]Center for Space Physics, Boston University, MA, USA

[3]Ionospheric Physics, Stoughton, MA, USA

[4]Space Vehicles Directorate, Air Force Research Laboratory, Albuquerque, NM, USA

Corresponding author: Deepak Kumar Karan (Deepak.Karan@lasp.colorado.edu)

Key Points:

- Maximum poleward shift ($\sim$11°) of EIA crests was observed between $\sim$15°W-5°W Glon coinciding with a penetration electric field

- Reversed C-shape Equatorial Plasma Bubbles (EPBs) extended to $\sim$$\pm$36° Mlat ($\sim$40°N and $\sim$30°S Glat) with apex altitudes reaching $\sim$4000 km

- EPBs at midlatitudes showed large westward tilts and zonal drifts that were quantified as a function of apex heights

Abstract

A coronal mass ejection (CME) erupted from the Sun on 21 April 2023 and created a G4 geomagnetic storm on 23 April. NASA's Global-scale Observations of the Limb and Disk (GOLD) imager observed bright Equatorial Ionization Anomaly (EIA) crests at ~25º Mlat, ~11º poleward from their average locations between ~15ºW-5ºW Glon. Reversed C-shape Equatorial Plasma Bubbles (EPBs) were observed reaching ~±36º Mlat (~40ºN and ~30ºS Glat) with apex altitudes ~4000 km and large westward tilts of ~52º. A latitude shear in the EPBs zonal motion was observed, with eastward motion near the equator and westward at mid-latitudes. Prompt penetration electric fields affected the postsunset pre-reversal enhancement at equatorial latitudes while disturbance dynamo-induced westward neutral winds and perturbed westward ion drifts over mid-latitudes contributed to the observed latitudinal shear in zonal drifts.

Plain Language Summary

A severe geomagnetic storm occurred on 23 April 2023. The effects of the storm on the nighttime equatorial and mid-latitude ionosphere are investigated using NASA's Global-scale Observations of the Limb and Disk (GOLD) measurements. GOLD observed bright, widely separated Equatorial Ionization Anomaly (EIA) crests between ~15ºW-5ºW Glon. Extreme Equatorial Plasma Bubbles (EPBs) reaching mid latitudes at ~40ºN and ~30ºS Glat with apex altitudes of ~4000 km at the magnetic equator were observed over these longitudes. The EPBs velocities were eastward at low latitudes, between the EIA crests, and reversed to westward near mid-latitudes. At mid-latitudes EPBs showed westward tilts that were larger than previous observations during similar geomagnetic conditions.

1 Introduction

The characteristics and variations of the Equatorial Ionization Anomaly (EIA) depend on several factors, including neutral winds, tides, electric fields, magnetic declination, pre-reversal enhancement (PRE), ion production and loss rates, and the subsolar point location (Eastes et al., 2023 and references therein). Other features observed in the same region are Equatorial Plasma Bubbles (EPBs), which are linked to factors like neutral winds, electric fields, conductivities, and plasma density, as noted in Karan et al., (2020, 2023b).

During quiet geomagnetic conditions, zonal drifts at the magnetic equator are eastward near the peak F region and slower at higher and lower altitudes. This causes the EPBs to shift westward at higher apex altitude and the EPB appear to be a reversed C-shape structure (Karan et al., 2020; 2023a; Kil et al., 2009; Martinis et al., 2003; Zalesak et al., 1982). Using data form an all-sky imager at Ascension Island (~14°W Glon, ~8°S Glat, ~18°S Mlat), Mendillo and Tyler (1983) formulated a relationship between the EPBs westward tilt and the local time, showing that the tilt increased as the night progressed.

Geomagnetic storms alter winds and electric fields through prompt penetration electric field (PPEF) (Kelley et al., 2003) and disturbance dynamo electric fields (DDEF) (Blanc and Richmond, 1980; Fejer et al., 1979), thereby changing the EIA morphology (Abdu et al., 1991, 1995; Balan et al., 2018). Sometimes the electron density at night in the EIA crests latitudes increases due to the penetration of an eastward disturbance electric field (Takahashi et al., 1987; Balan et al., 2018). Furthermore, storm-generated equatorward winds can move up ionospheric layers to higher altitudes, where recombination occurs more slowly, resulting in larger EIA peak densities that decay more slowly (Lin et al., 2005). During storms, the EIA may expand polewards, displacing the crests to mid-latitudes. Karan et al., (2023a) observed an 8°-10° poleward shift of post-sunset EIA crests during a storm, attributed to an enhanced PRE driven by an increase in eastward PPEF, corroborated by ionosonde measurements that showed an increase in the height of the peak electron density, hmF2.

Geomagnetic storms can either promote or hinder the formation of EPBs (Aarons et al., 1991; Abdu et al., 1995; Cherniak & Zakharenkova, 2022; Martinis et al., 2005; Kil et al., 2016; Patra et al., 2016;). During some storms, the PRE is intensified, causing EPBs to ascend to higher apex altitudes with field lines reaching latitudes around ~30-40° Mlat (Aa et al., 2018, 2019; Martinis et al., 2015; Rajesh et al., 2022; Huba et al., 2023; Sousasantos et al., 2023). Zonal drifts at low and mid latitudes can become westward due to the disturbance dynamo westward neutral winds (Sutton et al., 2005), equatorward expansion of subauroral ion drifts (Ferdousi et al., 2019), or the influence of traveling ionospheric disturbances (TIDs) (Aa et al., 2019). These westward drifts can increase the EPBs' westward tilt but this has not been quantified under perturbed geomagnetic conditions.

In this work, we investigated the poleward expansion of EIA and reversed C-shape EPBs extending to mid-latitudes between ~15ºW-5ºW Glon during the 23 April 2023 geomagnetic storm, using NASA's Global-scale Observations of the Limb and Disk (GOLD) images. Relationships between the EPB's westward tilt and zonal drifts with apex altitude are established.

2 Data

This study utilizes nighttime partial disk images from the GOLD imager, situated in a geostationary orbit at 47.5ºW, featuring two identical and independent channels (A and B, CHA and CHB hereafter), capturing FUV wavelengths (~132-162 nm). The instrument and its observations are detailed in Eastes et al., (2017, 2019, 2020) and McClintock et al., (2020). The nighttime OI 135.6 nm emission is produced by recombination of atomic oxygen ions and electrons in the Earth's ionosphere. Since the emission rate varies approximately as the square of the electron density, it maximizes at the peak F layer which is assumed to be 300 km. GOLD takes images across the American, Atlantic, and West African longitudinal sectors between 19 and 22 LT.

Solar wind parameters, geomagnetic indices, and modeled ionospheric PPEF (Manoj and Maus, 2012) are used to provide context for the GOLD observations. Zonal ion drifts from a Defense Meteorological Satellite Program (DMSP) satellite are compared with GOLD-inferred EPB zonal drifts.

3 Results

Figure 1 presents GOLD observations of the EIA and EPBs on the storm night, 23-24 April 2023. Images are selected to cover all the longitudes and to avoid repetition at similar longitudes. All the images during 23 April 20:10 UT to 24 April 00:25 UT are available as Movie-M1 in the supporting information. The images in the top row (panels A-D) illustrate that the EIA crests are brighter, and EPBs, represented by dark bands extending through the EIA crests, are observed at longitudes to the east of ~ 30° W, while no EPBs are seen to the west of ~30° W (panels E-H). All the EPBs exhibit significant westward tilts on both hemispheres.

The geomagnetic conditions on 22-23 April 2023 are shown in Figure 2. Solar wind parameters are in panels A (magnetic field IMF Bz and electric field IEF Ey) and B (solar wind
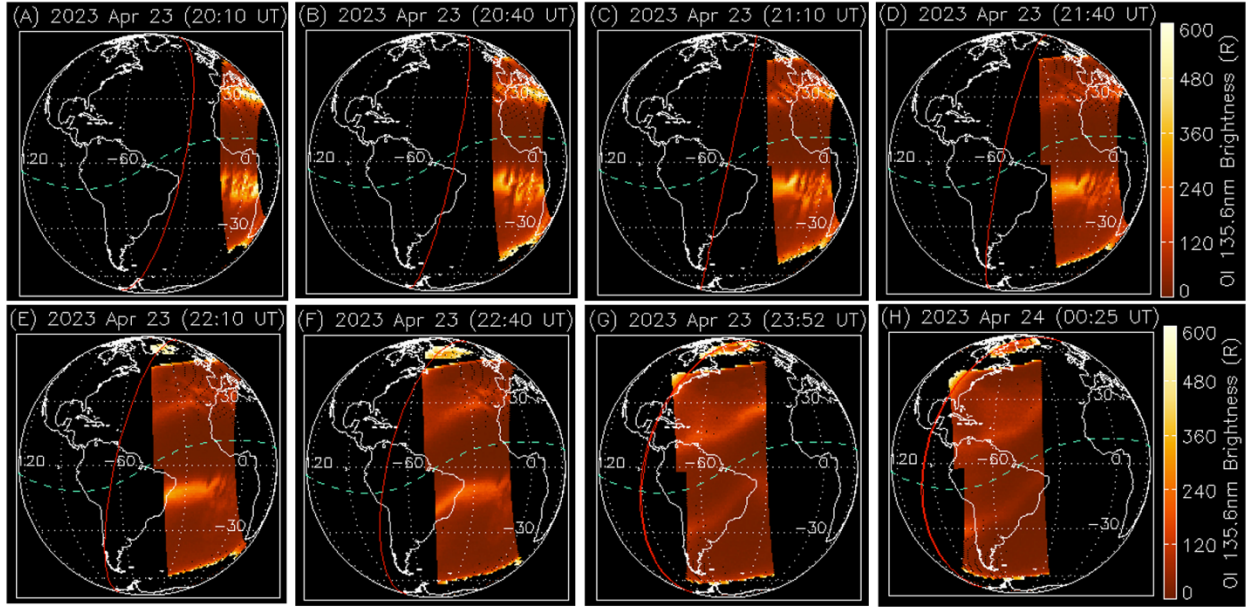
Figure 1. Nighttime 135.6 nm images captured by the GOLD imager on April 23-24, 2023. Highlighted are selective images covering all longitudes monitored by GOLD. The dashed green line and solid red line represent the geomagnetic equator and the sunset terminator, respectively.

proton density and speed). Panel C displays the equatorial geomagnetic index (SYM-H). The thick red line at the bottom of panel C indicates the times of GOLD's observations. The main phase of the storm commenced around 09:00 UT on 23 April and persisted until ~05:00 UT, when SYM-H reached a minimum value of ~ -220 nT. About 11 hrs after the initiation of the main phase, GOLD nighttime observations started as the SYM-H reached a minimum value of ~175 nT. At about 18 UT, Bz changed suddenly (density and speed also changed), reaching ~22 nT and maintaining this level for ~2 hrs. The 18-20 UT time range corresponds to post-sunset times in the longitudes ~15°W-5°E. These conditions led to the penetration of an E-field into equatorial latitudes.

To investigate the geomagnetic storm's effect on the EIA crests latitude values, we obtained the crests latitudes on the storm night (23-24 April). Panel A in Figure 3 displays the average and standard deviation of EIA crests latitudes (N in red and S in blue) obtained from all the images, following the method described in Eastes et al., (2023). Larger standard deviations, particularly near ~15°W, are a result of increased uncertainties during the calculation of EIA crests locations in the presence of EPBs. The red and blue solid lines indicate the average EIA crests latitudes during the previous geomagnetic quiet days (18 to 22 April). On the storm night, the EIA crests extended furthest between ~15°W-5°W Glon, with the N and S crests at ~27° and ~25° Mlat,

respectively. Panel B illustrates the differences between the storm night EIA crest latitudes and the

quiet time average values. Maximum poleward shifts of ~11º and 9º in the N and S EIA crests
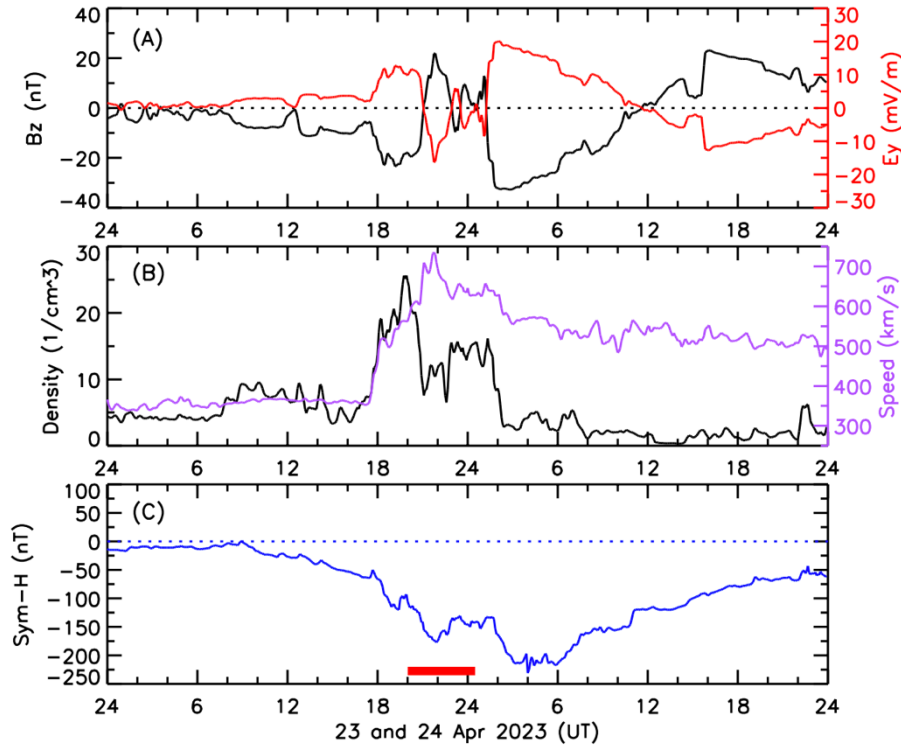

Figure 2. Solar wind parameters and geomagnetic indices on 23-24 April 2023. (A) IMF Bz and IEF Ey; (B) proton density and plasma flow speed, and (C) Sym-H. The thick horizontal red line indicates the timing of GOLD observations.
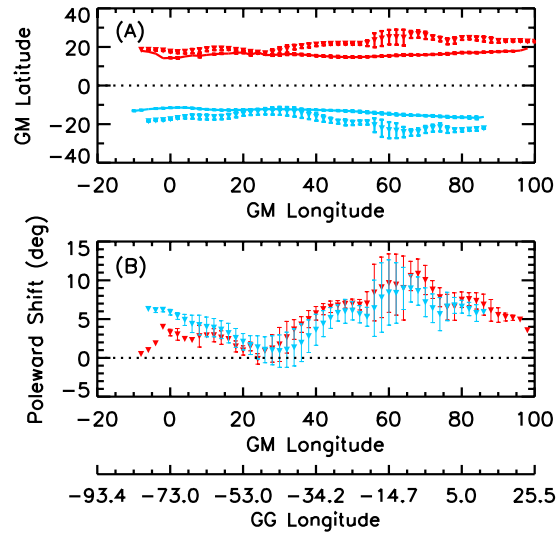

Figure 3. (A) EIA crests latitudes, North (red) and South (blue). 23 April shown as dashed lines and quiet time average as solid lines; (B) Relative shifts in EIA crests latitudes on 23 April 2023 compared to quiet time average with uncertainties.

136 were observed between ~15°W–5°W Glon.
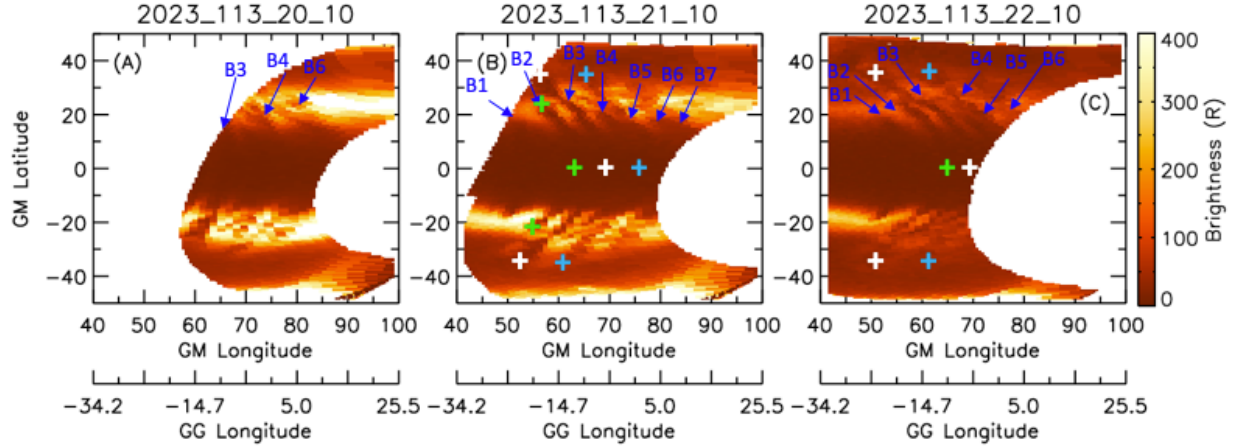

Figure 4. (A), (B), (C) combined CHA (N-hemisphere) and CHB (S-hemisphere) images at 20:10, 21:10, and 22:10 UT, respectively.

137

138   Panels A, B, and C in Figure 4 show the combined CHA and CHB images in quasi-dipole

139 (QD) coordinates (Laundal and Richmond, 2017) at 20:10, 21:10, and 22:10 UT, respectively,

140 encompassing seven EPBs (marked as B1 to B7) observed during this night. These EPBs exhibit

141 a westward tilt relative to the magnetic meridian and extend poleward through and beyond the EIA

142 crests. The foot points of B3 and B4 (indicated by white and cyan '+' symbols, respectively)

143 extended beyond ~±36° Mlat (~40°N and ~30°S Glat) (panels 4B and 4C), implying structures

144 with apex altitudes exceeding ~4000 km. Magnetic field lines were traced using the IGRF-13

145 model (Alken et al., 2021). EPB B2 appeared to merge with B3 at latitudes beyond the EIA crest

146 (panel 4C). The time sequence of the behavior of EPBs is shown as a movie Movie-M2 in the

147 supporting information. All seven EPBs were situated within ~15°W-0° Glon (~60° to 75° Mlon).

148 For a clear view of EPB locations near the magnetic equator, where the brightnesses were lower

149 compared to the EIA crests, panels 4A-C were replotted with a lower brightness scale in Figure

150 S1 in the supporting information. The bubbles separation at the equator was ~5°, which increased

151 to ~8° at the EIA crests latitudes.

152

153   The westward tilt angles of B2 and B3 at 22:10 UT are ~42° at ~16° Mlat, and ~52° at ~30°

154 Mlat. These tilts can be related to altitudinal/latitudinal shears in the zonal plasma drifts. Thus, we

155 tracked the EPBs drifts at several latitudes. The method for deriving EPBs' drift velocity is detailed

156 in Karan et al., (2020). EPBs were moving eastward near equatorial and low latitude regions and
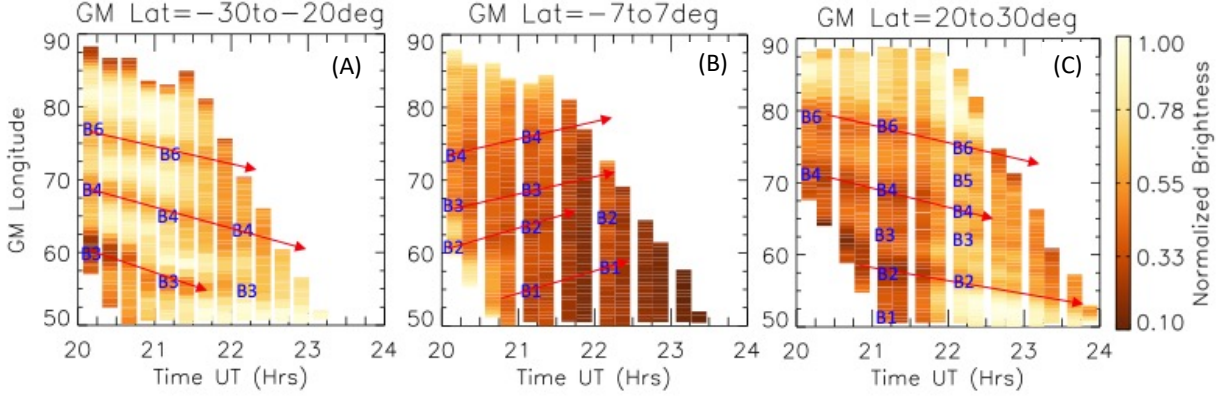
Figure 5. (A), (B), (C) longitudinal variations of normalized brightness obtained at different times as keograms for 30º-20ºS, 7ºS to 7ºN and 20º-30ºN latitude ranges, respectively.

157   westward at latitudes higher than ~±20º Mlat. Keograms in Figure 5 illustrate this behavior. Three

158   magnetic latitude ranges, 30º-20ºS, 7ºS-7ºN, and 20º-30ºN were selected. In an image (at a fixed

159   UT), within 30º-20ºS latitude range, the brightness at each longitude is averaged to obtain the

160   longitudinal variations of the brightnesses at that UT. To enhance visibility of the EPBs against

161   the varying background brightness, the brightness array was normalized to a maximum of 1. This

162   process was repeated for all the images, and the results were coplotted as a keogram in panel 5A.

163   Same method is followed to obtain keograms for 7ºS-7ºN and 20º-30ºN, shown in panels 5B and

164   5C, respectively. Different time gaps between the longitudinal stamps in the keograms are due to

165   varying latitudinal coverage of the images. EPBs longitudinal shifts are shown by red arrows. The

166   average zonal drifts of all EPBs during the observation periods is 120±15 m/s eastward within the

167   7ºS-7ºN latitudes (panel 5B), whereas within the latitude range of 20º-30ºN and 30º-20ºS, they

168   reversed and are 70±3 and 85±4 m/s westward, respectively.

169

170   **4 Discussion**

171   On 23 April 2023, we observed maximum poleward shifts of ~11º in the northern and ~9º

172   in the southern hemisphere EIA crests in between ~15º-5ºW Glon. In the same longitude sector,

173   reversed C-shape EPBs extending poleward beyond ±36º Mlat (~40ºN and ~30ºS Glat) were

174   detected. The poleward shifts of the EIA crests are similar to the ones reported by Karan et al.,

175   (2023a) at a larger longitude range of ~65º-35ºW Glon, during a geomagnetic storm weaker than

176   the one on 23 April 2023. The ionospheric response in that study showed that the peak altitude of

177   the ionospheric hmF2 layer increasing over those longitudes. The number of EPBs also increased,

178   as on 23 April 2023, but now the morphology shows extreme characteristics.
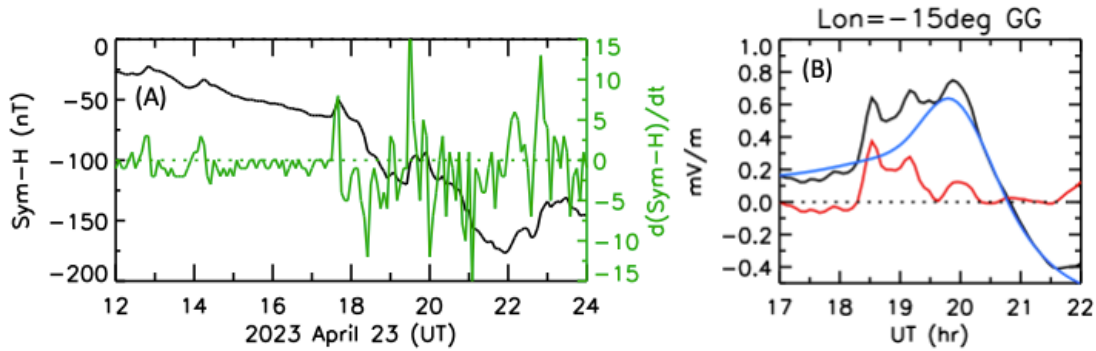
179

Figure 6. (A) Sym-H index in black and d(Sym-H)/dt in green during 12 to 24 UT on 23 April; (B) modeled total zonal electric field (black), PPEF (red), and quiet time electric field (blue) at 15°W Glon on 23 April.

180

The maximum poleward shifts of the EIA crests latitudes in between ~15°-5°W Glon (Figure 3) is likely due to an enhanced PRE (Abdu et al., 1991; Balan et al., 2018), This enhancement could be due to a penetration electric field. Sym-H and its rate of change, d(Sym-H)/dt, are shown in panel A of Figure 6. The rate of change of Sym-H showed a large negative excursion at ~18:30 UT with a maximum value of ~ -12 nT/5 min (~ -144 nT/hr). The sudden change in IMF Bz at ~18UT (panel 2A) and the sharp decrease in Sym-H at ~18-19 UT suggest a prompt penetration of an eastward electric field into the equatorial and low latitudes at this dusk sector (~15°W Glon) due to under-shielding conditions (Fejer et al., 1979). In the absence of electric field measurements over this longitude sector, the electric field model developed at Geomagnetism, CIRES (Cooperative Institute for Research in Environmental Sciences) (Manoj and Maus, 2012) was used. This model has been applied in other studies (Aa et al., 2019; Karan et al., 2023a; Spogli et al., 2021). Panel B shows the quiet time, prompt penetration (PPEF), and total electric fields in blue, red, and black lines, respectively. PPEF between ~18:15-20:15 UT contributed to ~2 hr extended PRE (peak value ~0.7 mV/m at ~20 UT). The maximum poleward shift in the EIA crests latitudes observed an hour after the peak PRE could be due to the transport time of plasma from equator to EIA crests (Karan et al., 2016, Karan and Pallamraju, 2020). A zonal electric field of ~0.7 mV/m produces an upward drift of ~32 m/s at this longitude. The PRE duration was ~1hr in the previous quiet days. For the mid latitude EPBs reported by Aa et al. (2019), the model total electric field was 0.9 mV/m with a duration of ~1hr. The longer duration

200 PRE in the present case (~2 hrs) could have enhanced plasma drift shifting the EIA crests further
201 poleward.

202

203   The long-duration PRE is also an important factor for the generation and maximum altitude
204 of the EPBs. At 20:10UT, just one hour after the sunset, GOLD detected a well-developed EPB
205 B3 already reaching an apex altitude of ~2000 km (Panel A in Figure 4). This implies that the
206 EPBs had upward drifts of ~500 m/s, an unusually large value that, has rarely been reported in the
207 past. For example, upward drifts ~1200 m/s were measured by Abdu et al. (2008), between 100-
208 1000 m/s by Aggson et al., (1992), and ~1200 m/s by Hysell (1994). While we have no means to
209 effectively measure the upward drift, some inferences can be made from the poleward motion of
210 EPBs as observed by GOLD. By measuring the poleward motion of B1, B2, B3, and B4 between
211 18°-24° Mlat an average speed of ~130 m/s is obtained, which is similar to ~110 m/s reported in
212 Martinis et al., (2015) who investigated EPBs reaching midlatitudes. This poleward drift can be
213 interpreted as a vertical drift near the magnetic equator with an eastward electric field of ~3.3
214 mV/m. In the present case, the long-duration PRE could have moved the F layer to high altitudes
215 and caused the generation of EPBs with deep density depletion.

216

217   Along with the expansion of the EPBs to higher altitudes/latitudes, their drift directions
218 changed from eastward (near the magnetic equator) to westward (at latitudes higher than ~$\pm 20^{o}$
219 Mlat) (Figure 5). The latitude where the EPB drifts reversed can be investigated by plotting the
220 keograms in 5° latitude ranges, shown in Figure 7. Panels 7A (10°-15°N) and 7G (10°-15°S) show
221 that, at ~ 22 UT EPB's longitude shift with time becomes flat when compared to the variation
222 within 7°S to 7°N latitude range (panel 5B). This indicates that the EPBs drifts slowed down from
223 equatorial to low latitude regions. The reverse in EPBs' longitude shift direction with time around

224   ±20° Mlat indicates that EPBs motion changed from eastward to westward close or below this
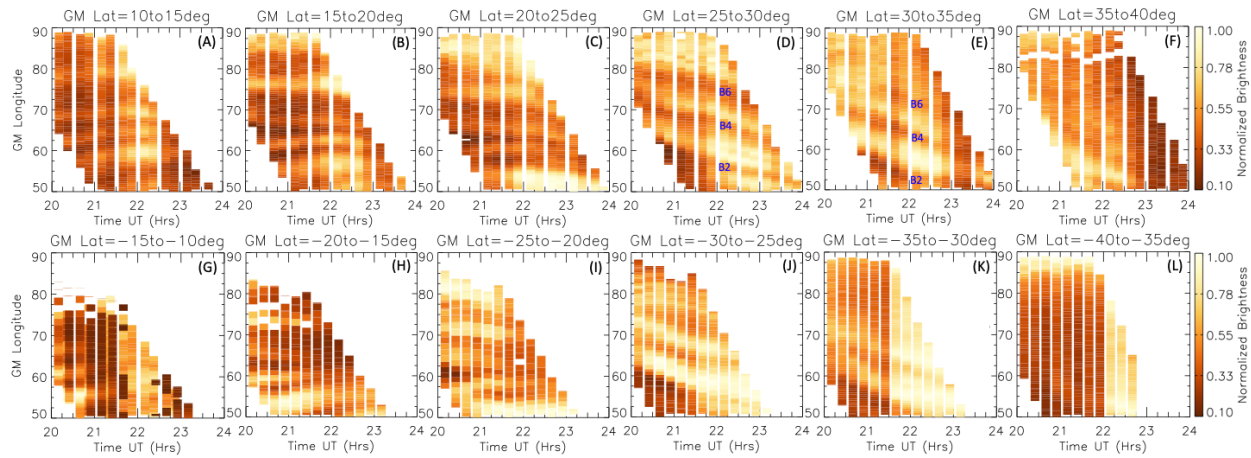225   latitude.

Figure 7. Same as Figure 5 (Panels A-C but at 5° latitude ranges. The transition in the EPBs eastward motion at equatorial and low latitudes to westward at mid latitudes can be seen close to ±20° Mlat, between panels B-C and H-I.

226

227   The reduction and reversal of eastward drifts from low to midlatitudes has usually been
228   related to disturbance dynamo effects on zonal winds (Blanc and Richmond, 1980; Fejer et al.,
229   1979; Sutton et al., 2005). Recently, Huang et al., (2021) show subauroral polarization streams
230   (SAPS) effects reaching low latitudes. Figure 8 displays the net change (or difference) in zonal ion
231   drifts between the storm and a quiet day (22 April), used as reference, as measured by DMSP F17.
232   Panel 8a shows the difference in zonal ion drifts between 23 and 22 April. DMSP F17 observations
233   at 18:30 LT at certain longitudes is interpolated for other UTs. Panel 8b shows the values at 18
234   and 19UT, which correspond to longitudes ~7.5°E and ~7.5°W on Apr 23, where westward tilted
235   EPBs were observed. Reductions of ~30 m/s, ~60 m/s, and ~100 m/s at ~0°, ~15°, and ~30° Mlat,
236   respectively, were observed. The westward drifts of ~800 m/s and ~500 m/s at subauroral latitudes
237   of ~55° N and ~55° S indicate SAPS effects, potentially penetrating to middle and low latitudes,
238   contributing to the westward drifts measured. Utilizing GOLD observations, we calculated the
239   difference in EPBs' zonal drifts between 23 and 22 April. A reduction of ~90 m/s in EPBs' zonal
240   drifts was identified at ~15° Mlat and ~7°W Glon (location of B3) around 19 UT, result that is
241   similar with the DMSP reduction observed at ~15° Mlat (60 m/s). Thus, the reversal of EPBs'
242   zonal drifts, transitioning from eastward at low latitudes to westward at middle latitudes, as

243 observed by GOLD, agrees with the latitude profile of the difference in zonal plasma drifts
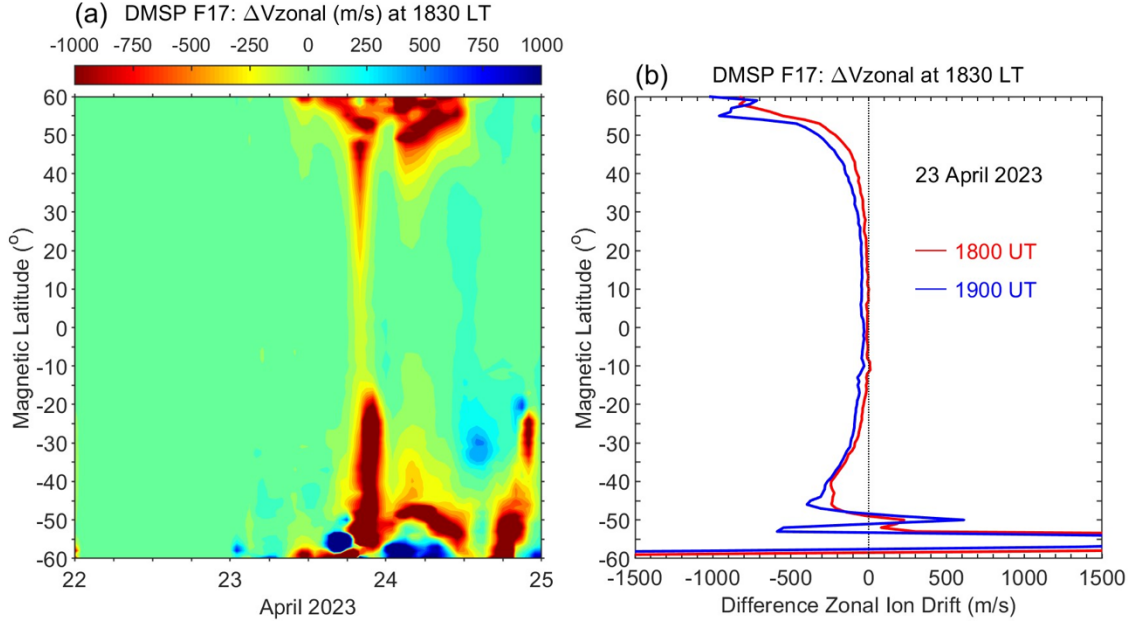244 measured by DMSP.

245

Figure 8. (a) Difference zonal ion drifts measured by the DMSP F17 satellite at ~18:30 LT considering April 22 as a reference and (b) Latitudinal profile of the difference zonal ion drifts at 18 and 19 UT.

246

247 As mentioned earlier, the EPBs appeared as reversed C-shape structures, related to their
248 westward tilts. GOLD measures EPBs in a latitude and longitude plane, off the magnetic equator,
249 at a fixed height of 300 km. Focusing on bubble B3 the tilt seems to change with latitude. At 22:10
250 UT around 35°N Glat (~30° Mlat) and 25°N Glat (~16° Mlat) the tilts are ~52° and ~42° westward.
251 Considering that the magnetic declination at these locations are ~5° and 1.5°, then B3 is tilted ~47°
252 and ~40.5° with respect to (w.r.t.) the magnetic meridian. Bubble B2 shows a tilt of 40°, or ~37°
253 w.r.t. the magnetic meridian. In comparison, the westward tilt w.r.t. magnetic meridian from Aa
254 et al., (2019) were ~25° and ~11° at similar magnetic latitudes and from Martinis et al., (2015), it
255 was ~22° at ~30° Mlat. Geomagnetic conditions were similar, with Sym-H reaching ~ -110 nT in
256 these studies. Because EPBs exhibit a plasma flux-tube nature along the magnetic field lines, an
257 alternative method for measuring tilt involves mapping them into the magnetic equatorial plane.
258 This representation depicts an EPB in an altitude-magnetic longitude plane, where altitude
259 corresponds to the field line's apex height, and is linked to the magnetic latitude at the field line's

12

260   footpoint. In this plane, B3 reaches ~36º Mlat with a break or kink in the shape of the bubble

261   between ~24-25 º Mlat. The westward tilt for the upper portion of B3 is ~25 º and for the lower

262   part ~32 º. B2 reaches ~25º Mlat with a westward tilt of ~34º.

263

264   Mendillo and Tyler (1983) (M&T) used this approach to quantify the EPBs westward tilt

265   (W) as a function of local time as observed from Ascension Island using gound-based imaging.

266   The apex altitudes they observed ranged from 400-1200 km. For the relatively geomagnetic quiet

267   conditions prevalent during their observations, they found:

268       $W = 0.15 \, (LT-18.3)$ (1)

269   W is the westward shift in degrees of magnetic longitude per 100 km in apex altitude. Applying

270   this formula to EPBs B2 and B3 of Figure 4, we obtain $W = 0.43$. Expressed as the angle between

271   the orientation of the EPB and the magnetic meridian, this becomes 23º.

272

273   We next compare this result with the measured tilt values of B2 and B3. At 20º Mlat B3

274   has $W_{B3l} = 0.63$ (corresponding to a tilt angle of 32º), while at 30º Mlat B3 has $W_{B3u} = 0.47$

275   (corresponding to 25º). For B2, which does not extend much past 25º Mlat, $W_{B2} = 0.67$

276   (corresponding to 34º). Since the GOLD observations occurred during a geomagnetic storm, it is

277   not surprising that the westward tilts exceed those observed by M&T. Both studies found EPBs

278   with westward tilts. Under storm conditions, however, we observe nighttime zonal drifts at low

279   and mid latitudes that display a reduction or even a reversal of the typical eastward motion to

280   westward. Consequently, EPBs observed during storm conditions may exhibit a more 'compressed'

281   reversed C-shape, which is precisely what GOLD is measuring.

282

283   If the westward tilt increases linearly following equation (1), M&T obtained an expression

284   for the altitude dependence for an effective westward drift, or reduction in the overall eastward

285   drift, V'(h) as

286       $V'(h) = 0.0464(1+h/R_E)$ (2)

287   Where 0.0464, in (m/s)/km units, is the product of the slope, 0.15 (measured in degrees of magnetic

288   longitude per 100 km vertical height) from (1), and a constant 0.31 (result of geometric factors

289   used in the calculation). At 300 km V'(300) = 0.049 m/s/km. This value represents the shear in

290   altitude of the zonal drifts from a height of 300 km. An eastward drift at 700 km apex height (12.5º

291   Mlat) would lag the drift at 300 km by 0.049*(700-300) ~ 20 m/s. Using an imager with a field of

292   view of ~ 47° located in Maui, Hawaii, Makela and Kelley (2002) applied the M&T approach to

293   EPBs and obtained an average shear value of 0.05 m/s/km. But when they calculated the shear by

294   computing the velocities obtained at each height, a value of 0.1 m/s/km was obtained. This

295   discrepancy was not explained.

296

297   Figure 9 shows the calculated EPBs' average zonal drift velocities for each of the latitude

298   ranges (as shown in Figure 7) as a function of apex altitudes (or magnetic latitudes). Below ~1500

299   km apex height the larger slope (compared to heights above 1500 km) indicating a faster decrease

300   (with latitudes) in the drift speeds. The average zonal drifts of the EPBs at apex altitudes close to

301   300 km (magnetic equator), 700 km, and 1000 km, are 120 m/s, 62 m/s, and 25 m/s, respectively.

302   The transition from eastward to westward drift occurs around 1000 km (17.5° Mlat). According to

303   (2) the transition height (where the lag is equal to ~120 m/s) should occur at ~2750 km, much

304   higher than the height observed. Like the underestimation in the westward tilt W from (1), V' is

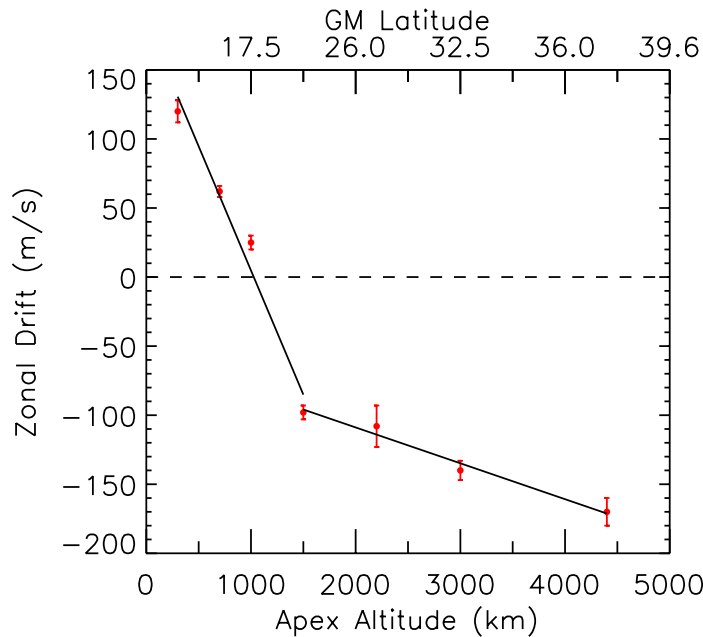305   also showing a weak altitude variation.

Figure 9. EPBs' average zonal drifts (m/s) for each latitude ranges (shown in Figure 7) with corresponding apex altitudes are shown. The transition from east to west occurred at ~1200 km (~20° Mlat).

306

307   The shear V'(300 km) for the GOLD data can be obtained from the slope of the fitted line

308   to the data between 300 to 1500 km, shown in Figure 9. This slope is V'_{GOLDl} = 0.179 m/s/km.

309   This shear can also be obtained by considering the average westward tilt of the EPBs measured in

310   GOLD images. The westward tilt W_{GOLD} at 20º Mlat can be calculated as the shift in magnetic

311   longitude (5º) divided by the extent of the bubble (920 km), equal to – 0.63. When this value is

312   multiplied by 0.31, a shear of 0.195 m/s/km is obtained, close to the slope of the fitted curve in

313   Figure 9. This result indicates a good agreement between the shears obtained by the two methods,

314   something that was not observed in the Makela and Kelley (2003) study.

315

316   With these new shear values (0.179 and 0.195), drifts at 1000 and 1500 km will lag the

317   drift at 300 km by 112 (136) m/s and 192 m/s (234), respectively. The drifts at these heights will

318   be 8 (-12) m/s and -70 (-114) m/s. The transition from eastward to westward occur at the observed

319   height range of ~1000-1100 km. The upper part of B3 shows a different shear V'_{GOLDu} = 0.026

320   m/s/km, so the height variation of the drifts is weaker, as seen in Figure 8. We can summarize the

321   results that relate westward tilts and height variation of zonal drifts of B3 as:

322   W_{GOLDl} = 0.63
323   Vel_l = 185 m/s - 0.179*h   for h < 1500 km   (3)

324
325   and
326
327   W_{GOLDu} = 0.47
328   Vel_u = -57 -0.026*h   for h > 1500 km   (4)

329

330   Therefore, we obtained average expressions for the westward tilt and zonal drifts as a function of

331   apex height. At lower altitudes, below ~1500 km, the height variation of zonal drifts is large, but

332   above ~1500 km it proceeds at a smaller rate, but large westward drifts are measured. This

333   indicates a different response of the ionosphere at low latitudes when compared to mid latitudes.

334

335   **5 Summary**

336   This paper investigated the EIA and EPB characteristics as observed by the NASA GOLD imager

337   during the 23 April 2023 geomagnetic storm. The perturbed geomagnetic conditions prevailing on

338   that night were responsible for the emergence of EPBs characterized by significant westward tilts

339   and substantial latitudinal shears in the zonal drift velocities. The key findings are:

340   (i)   Maximum (~11º) poleward shifts of both EIA crests latitudes and reversed C-shape
341   EPBs were observed at ~15º-5ºW Glon. A modeled eastward PPEF lasted for ~2hrs
342   and extended the PRE, moving plasma to higher latitudes.

343   (ii)   EPBs reached beyond ±36º Mlat (~40º N and ~30ºS Glat), implying structures with
344   apex altitudes exceeding ~4000 km. EPBs showed westward tilts of ~52º at ~30º Mlat
345   and ~42º at ~16º Mlat, higher than previously reported cases under similar geomagnetic
346   conditions.

347   (iii) EPBs zonal drifts showed a strong latitudinal shear, with eastward drifts of 120±15 m/s
348   over equatorial latitudes and westward drifts of 70±3 m/s at N and 85±4 m/s at S EIA
349   crests.

350   (iv) Inferred poleward drifts obtained by GOLD images were used to estimate an effective
351   eastward electric field of ~3.3 mV/m near the magnetic equator.

352   (v)   The reversal of EPBs' zonal drifts as observed by GOLD, agrees with the latitude
353   profile of the difference in zonal plasma drifts measured by DMSP.

354   (vi) We obtained expressions for the westward tilt of EPBs and the apex height (or magnetic
355   latitude) dependence of their zonal drifts. Results show a linear variation up to ~1500
356   km (~22.5º Mlat), with smaller shears observed at higher latitudes.

357

360   **Open Research**

361   The GOLD data are available from the GOLD Science Data Center
362   (https://gold.cs.ucf.edu/data/search/). The solar wind parameters and geomagnetic indices are
363   taken from the NASA GSFC SPDF OMNI website

364   (https://omniweb.gsfc.nasa.gov/form/omni_min.html). Model ionospheric electric fields are

365   obtained from (https://geomag.colorado.edu/real-time-model-of-the-ionospheric-electric-fields).

366

367   **References**

368   Aa, E., Huang, W., Liu, S., Ridley, A., Zou, S., Shi, L., Chen, Y., Shen, H., Yuan, T., Li, J., &

369   Wang, T. (2018). Midlatitude plasma bubbles over China and adjacent areas during a magnetic

370   storm on 8 September 2017. Space Weather, 16, 321– 331.

371   https://doi.org/10.1002/2017SW001776

372

373   Aa, E., Zou, S., Ridley, A. J., Zhang, S.-R., Coster, A. J., Erickson, P. J., Liu, S., & Ren, J.

374   (2019). Merging of storm-time midlatitude traveling ionospheric disturbances and equatorial

375   plasma bubbles. Space Weather, 17, 285– 298. https://doi.org/10.1029/2018SW002101

376

377   Aarons, J. (1991). The role of the ring current in the generation or inhibition of equatorial F layer

378   irregularities during magnetic storms. Radio Science, 26(4), 1131–1149.

379   https://doi.org/10.1029/91RS00473

380

381   Abdu, M. A., Sobral, J. H. A., de Paula, E. R., & Batista, I. S. (1991). Magnetospheric

382   disturbance effects on the Equatorial Ionization Anomaly (EIA)—An overview. Journal of

383   Atmospheric and Terrestrial Physics, 53, 757–771. https://doi.org/10.1016/0021-9169(91)90126-

384   R.

385   Abdu, M. A., I. S. Batista, G. O. Walker, J. H. A. Sobral, N. B. Trivedi, and E. R. de Paula (1995),

386   Equatorial ionospheric fields during magnetospheric disturbances: Local time/longitudinal

387   dependences from recent EITS Campaigns, J. Atmos. Sol. Terr. Phys., 57, 1065– 1083.

388

389   Abdu, M. A., et al. (2008), Abnormal evening vertical plasma drift and effects on ESF and EIA

390   over Brazil-South Atlantic sector during the 30 October 2003 superstorm, J. Geophys. Res., 113,

391   A07313, doi:10.1029/2007JA012844.

392

393   Alken, P., Thébault, E., Beggan, C.D. et al. International Geomagnetic Reference Field: the

394   thirteenth generation. Earth Planets Space 73, 49 (2021). https://doi.org/10.1186/s40623-020-

395   01288-x

396

397   Aggson, T. L., Maynard, N. C., Hanson, W. B., and Saba, J. L. (1992), Electric field

398   observations of equatorial bubbles, J. Geophys. Res., 97(A3), 2997– 3009,

399   doi:10.1029/90JA02356.

400

401   Anderson, D., and Haerendel, G. (1979), The motion of depleted plasma regions in the equatorial

402   ionosphere, J. Geophys. Res., 84(A8), 4251–4256, doi:10.1029/JA084iA08p04251.

403   Balan N., Liu L. B., and Le H. J. (2018). A brief review of equatorial ionization anomaly and

404   ionospheric irregularities. Earth Planet. Phys., 2(4), 257–275. http://doi.org/10.26464/epp2018025

405

406   Blanc, M., and Richmond, A. D. (1980). The ionospheric disturbance dynamo. J. Geophys. Res.,

407   85(A4), 1669–1686. https://doi.org/10.1029/JA085iA04p01669

408   Cherniak, I., & Zakharenkova, I. (2022). Development of the storm-induced ionospheric

409   irregularities at equatorial and middle latitudes during the 25–26 August 2018 geomagnetic storm.

410   Space Weather, 20, e2021SW002891. https://doi.org/10.1029/2021SW002891

411   Eastes, R.W., McClintock, W.E., Burns, A.G. et al. (2017), The Global-Scale Observations of the

412   Limb and Disk (GOLD) Mission. Space Sci Rev 212, 383–408, doi:10.1007/s11214-017-0392-2.

413   Eastes, R. W., S. C. Solomon, R. E. Daniell, D. N. Anderson, A. G. Burns, S. L. England, C. R.

414   Martinis, and W. E. McClintock (2019), Global-scale observations of the equatorial ionization

415   anomaly. Geophysical Research Letters, 46, 9318–9326, https:// doi.org/10.1029/2019GL084199.

416   Eastes, R. W., McClintock, W. E., Burns, A. G., Anderson, D. N., Andersson, L., Aryal, S., et al.

417   (2020). Initial Observations by the Global-scale Observations of the Limb and Disk (GOLD)

418   mission. Journal of Geophysical Research: Space Physics, 125, e2020JA027823.

419   https://doi.org/10.1029/2020JA027823.

420 Eastes, R. W., Karan, D. K., Martinis, C., Daniell, R. E., Gan, Q., Burns, A. G., & McClintock,

421 W. E. (2023). GOLD observations of longitudinal variations in the nighttime equatorial ionization

422 anomaly (EIA) crests' latitudes. Journal of Geophysical Research: Space Physics, 128,

423 e2022JA031007. https://doi.org/10.1029/2022JA031007

424

425 Fejer, B. G., C. A. Gonzales, D. T. Farley, M. C. Kelley, and R. F. Woodman (1979), Equatorial

426 electric fields during magnetically disturbed conditions 1. The effect of the interplanetary

427 magnetic field, J. Geophys. Res., 84 (A10), 5797–5802, doi:10.1029/JA084iA10p05797.

428

429 Ferdousi, B., Nishimura, Y.,Maruyama,N., & Lyons, L. R. (2019). Subauroral neutral wind

430 driving and its feedback to SAPS during the 17March 2013 geomagnetic storm. Journal of

431 Geophysical Research: Space Physics, 124, 2323–2337. https://doi.org/10.1029/2018JA026193

432

433 Huang, C.-S., Zhang, Y., Wang, W., Lin, D., & Wu, Q. (2021). Low-latitude zonal ion drifts and

434 their relationship with subauroral polarization streams and auroral return flows during intense

435 magnetic storms. Journal of Geophysical Research: Space Physics, 126, e2021JA030001.

436 https://doi.org/10.1029/2021JA030001

437

438 Huba, J. D., Becker, E., & Vadas, S. L. (2023). Simulation study of the 15 January 2022 Tonga

439 event: Development of super equatorial plasma bubbles. Geophysical Research Letters, 50,

440 e2022GL101185. https://doi.org/10.1029/2022GL101185

441

442 Hysell, D. L., Kelley, M. C., Swartz, W. E., and Farley, D. T. (1994), VHF radar and rocket

443 observations of equatorial spread F on Kwajalein, J. Geophys. Res., 99(A8), 15065– 15085,

444 doi:10.1029/94JA00476.

445

446 Karan, D. K., D. Pallamraju, K. A. Phadke, T. Vijayalakshmi, T. K. Pant, and S. Mukherjee

447 (2016), Electrodynamic influence on the diurnal behavior of neutral daytime airglow emissions,

448 Ann. Geophys., 34, 1019–1030, doi:10.5194/angeo-34-1019-2016.

449

Karan, D. K., & Pallamraju, D. (2020). On estimation of daytime equatorial vertical (E × B) plasma drifts using optical neutral dayglow emission measurements. Journal of Geophysical Research: Space Physics, 125, e2019JA026775. https://doi.org/10.1029/2019JA026775

Karan, D. K., Daniell, R. E., England, S. L., Martinis, C. R., Eastes, R. W., Burns, A. G., & McClintock, W. E. (2020). First zonal drift velocity measurement of equatorial plasma bubbles (EPBs) from a geostationary orbit using GOLD data. J. Geophys. Res. Space Physics, 125, e2020JA028173, doi:10.1029/2020JA028173

Karan, D. K., Eastes, R. W., Daniell, R. E., Martinis, C. R., & McClintock, W. E. (2023a). GOLD mission's observation about the geomagnetic storm effects on the nighttime equatorial ionization anomaly (EIA) and equatorial plasma bubbles (EPB) during a solar minimum equinox. Space Weather, 21, e2022SW003321. https://doi.org/10.1029/2022SW003321

Karan, D. K., Eastes, R. W., Martinis, C. R., Daniell, R. E., Solomon, S. C., & McClintock, W. E. (2023b). Unique combinations of differently shaped equatorial plasma bubbles occurring within a small longitude range. Journal of Geophysical Research: Space Physics, 128, e2023JA031625. https://doi.org/10.1029/2023JA031625.

Kelley, M. C., Makela, J. J., Chau, J. L., and Nicolls, M. J. (2003), Penetration of the solar wind electric field into the magnetosphere/ionosphere system, Geophys. Res. Lett., 30, 1158, doi:10.1029/2002GL016321, 4.

Kil, H., R. A. Heelis, L. J. Paxton, and S.-J. Oh (2009), Formation of a plasma depletion shell in the equatorial ionosphere, J. Geophys. Res., 114, A11302, doi:10.1029/2009JA014369.

Kil, H., W. K. Lee, L. J. Paxton, M. R. Hairston, and G. Jee (2016), Equatorial broad plasma depletions associated with the evening prereversal enhancement and plasma bubbles during the 17 March 2015 storm, J. Geophys. Res. Space Physics, 121, 10,209–10,219, doi:10.1002/2016JA023335.

479   Laundal, K. M., and Richmond, A. D. (2017) Magnetic Coordinate Systems, Space Sci Rev, 206,

480   27-59. https://doi.org/10.1007/s11214-016-0275-y

481

482   Lin, C. H., Richmond, A. D., Heelis, R. A., Bailey, G. J., Lu, G., Liu, J. Y., Yeh, H. C., and Su,

483   S. Y. (2005). Theoretical study of the low- and midlatitude ionospheric electron density

484   enhancement during the October 2003 superstorm: Relative importance of the neutral wind and

485   the electric field. J. Geophys. Res., 110(A12), A12312. https://doi.org/10.1029/2005JA011304

486   Makela, J. J., and Kelley, M. C. (2003), Field-aligned 777.4-nm composite airglow images of

487   equatorial plasma depletions, Geophys. Res. Lett., 30, 1442, doi:10.1029/2003GL017106, 8.

488   Manoj, C., and S. Maus (2012), A real-time forecast service for the ionospheric equatorial zonal

489   electric field, Space Weather,10, S09002, doi:10.1029/2012SW000825

490

491   Martinis, C., Eccles, J. V., Baumgardner, J., Manzano, J., & Mendillo, M. (2003). Latitude

492   dependence of zonal plasma drifts obtained from dual-site airglow observations. Journal of

493   Geophysical Research, 108(A3), 1129. https://doi.org/10.1029/2002JA009462

494   Martinis, C. R., Mendillo, M. J., & Aarons, J. (2005). Toward a synthesis of equatorial spread F

495   onset and suppression during geomagnetic storms. Journal of Geophysical Research, 110(A7),

496   A07306. https://doi.org/10.1029/2003JA010362

497   Martinis, C., J. Baumgardner, M. Mendillo, J. Wroten, A. Coster, and L. Paxton (2015), The night

498   when the auroral and equatorial ionospheres converged, J. Geophys. Res. Space Physics, 120,

499   8085–8095, doi:10.1002/2015JA021555.

500   Mendillo, M., and Tyler, A. (1983), Geometry of depleted plasma regions in the equatorial

501   ionosphere, J. Geophys. Res., 88(A7), 5778– 5782, doi:10.1029/JA088iA07p05778.

502   McClintock, W. E., Eastes, R. W., Beland, S., Bryant, K. B., Burns, A. G., Correira, J., et al (2020).

503   Global-scale Measurements of the Limb and Disk (GOLD) Mission Implementation: 2.

504   Observations, Data Pipeline and Level 1 Data Products. Journal of Geophysical Research: Space

505   Physics, 125, e2020JA027809. https://doi.org/10.1029/2020JA027809.

506

507 Ossakow, S. L., and Chaturvedi, P. K. (1978), Morphological studies of rising equatorial spread

508 F bubbles, J. Geophys. Res., 83(A5), 2085–2090, doi:10.1029/JA083iA05p02085.

509

510 Patra, A. K., P. P. Chaitanya, N. Dashora, M. Sivakandan, and A. Taori (2016), Highly localized

511 unique electrodynamics and plasma irregularities linked with the 17 March 2015 severe magnetic

512 storm observed using multitechnique common-volume observations from Gadanki, India, J.

513 Geophys. Res. Space Physics, 121, 11,518–11,527, doi:10.1002/2016JA023384.

514 Rajesh, P. K., Lin, C. C. H., Lin, J. T., Lin, C. Y., Liu, J. Y., Matsuo, T., et al. (2022). Extreme

515 poleward expanding super plasma bubbles over Asia-Pacific region triggered by Tonga volcano

516 eruption during the recovery-phase of geomagnetic storm. Geophysical Research Letters, 49,

517 e2022GL099798. https://doi.org/10.1029/2022GL099798

518 Sousasantos, J., Gomez Socola, J., Rodrigues, F.S. et al. Severe L-band scintillation over low-to-

519 mid latitudes caused by an extreme equatorial plasma bubble: joint observations from ground-

520 based monitors and GOLD. Earth Planets Space 75, 41 (2023). https://doi.org/10.1186/s40623-

521 023-01797-5

522 Spogli., L, D. Sabbagh, M. Regi, C. Cesaroni, L. Perrone, L. Alfonsi, D. Di Mauro, S. Lepidi, S.

523 A. Campuzano, D. Marchetti, A. Santis, A. Malagnini, C. Scotto, G. Cianchini, Xu Hui Shen, A.

524 Piscini, A. Ippolito, (2021). Ionospheric Response Over Brazil to the August 2018 Geomagnetic

525 Storm as Probed by CSES-01 and Swarm Satellites and by Local Ground-Based Observations,

526 Journal of Geophysical Research: Space Physics, 10.1029/2020JA028368, 126, 2.

527 Sutton, E. K., Forbes, J. M., and Nerem, R. S. (2005), Global thermospheric neutral density and

528 wind response to the severe 2003 geomagnetic storms from CHAMP accelerometer data, J.

529 Geophys. Res., 110, A09S40, doi:10.1029/2004JA010985.

530

531 Takahashi, T., H. Oya, S. Watanabe (1987), Ionospheric disturbances induced by substorm

532 associated electric fields in the low-latitude F-region, J. Geomag. Geoelecric, 39, 187-209,

533 https://doi.org/10.5636/jgg.39.187

534

535   Zalesak, S.T., Ossakow, S.L., Chaturvedi, P.K., (1982), Nonlinear equatorial spread F: The effect

536   of neutral winds and background Pedersen conductivity. J. Geophys. Res 87, 151.

537   https://doi.org/10.1029/ 93ja00762.